SANDIA REPORT
SAND2014-20608
Unlimited Release
December and 2014

Computational and Experimental Characterization of Aluminum Nitride-Silicon Carbide Thin Film Composites for High Temperature Sensor Applications

Benjamin A. Griffin, Scott D. Habermehl, Peggy J. Clews, Sasha Summers, and Sukwon Choi

Prepared by
Sandia National Laboratories
Albuquerque, New Mexico 87185 and Livermore, California 94550

Sandia National Laboratories is a multi-program laboratory managed and operated by Sandia Corporation, a wholly owned subsidiary of Lockheed Martin Corporation, for the U.S. Department of Energy's National Nuclear Security Administration under contract DE-AC04-94AL85000.

Issued by Sandia National Laboratories, operated for the United States Department of Energy by Sandia Corporation.

Available to DOE and DOE contractors from
U.S. Department of Energy
Office of Scientific and Technical Information
P.O. Box 62
Oak Ridge, TN 37831

Telephone: (865) 576-8401
Facsimile: (865) 576-5728
E-Mail: reports@adonis.osti.gov
Online ordering: http://www.osti.gov/bridge

Available to the public from
U.S. Department of Commerce
National Technical Information Service
5285 Port Royal Rd.
Springfield, VA 22161

Telephone: (800) 553-6847
Facsimile: (703) 605-6900
E-Mail: orders@ntis.fedworld.gov
Online order: http://www.ntis.gov/help/ordermethods.asp?loc=7-4-0#online

SAND2014-20608
Unlimited Release
December 2014

Computational and Experimental Characterization of Aluminum Nitride-Silicon Carbide Thin Film Composites for High Temperature Sensor Applications

Benjamin A. Griffin
1719
Scott D. Habermehl
1747
Peggy J. Clews
1746
Sandia National Laboratories
P.O. Box 5800
Albuquerque, New Mexico 87185-MS1069

Abstract

A number of important energy and defense-related applications would benefit from sensors capable of withstanding extreme temperatures (>300˚C). Examples include sensors for automobile engines, gas turbines, nuclear and coal power plants, and petroleum and geothermal well drilling. Military applications, such as hypersonic flight research, would also benefit from sensors capable of 1000˚ C. Silicon carbide (SiC) has long been recognized as a promising material for harsh environment sensors and electronics. Yet today, many advanced SiC MEMS are limited to lower temperatures because they are made from SiC films deposited on silicon wafers. Other limitations arise from sensor transduction by measuring changes in capacitance or resistance, which require biasing or modulation schemes that can withstand elevated temperatures. We circumvented these issues by developing sensing structures directly on SiC wafers using SiC and aluminum nitride (AlN), a high temperature capable piezoelectric material, thin films.

ACKNOWLEDGMENTS

This work was funded under LDRD Project Number165711 and Title "Computational and Experimental Characterization of Aluminum Nitride-Silicon Carbide Thin Film Composites for High Temperature Sensor Applications".

CONTENTS

FIGURES

TABLES

Nomenclature

AlN	aluminum nitride
SiC	silicon carbide
MEMS	microelectromechanical systems
LPCVD	low pressure chemical vapor deposition
DCS	dichlorosilane (SiH_2Cl_2)
DCE	dichloroethylene ($C_2H_2Cl_2$)
CMP	chemical mechanical polish

1. INTRODUCTION

One of the fundamental objectives of MEMS technology is to create sensors and actuators possessing bandwidth and spatial resolution that is often not possible with mainstream mechanical fabrication techniques. The limited survivability of silicon-based MEMS sensors in high-temperature and harsh environments has caused researchers to investigate other materials for high-temperature capable MEMS-based sensors. Examples of MEMS materials for harsh environments include SiC, diamond, sapphire, and AlN.

Researchers have been investigating SiC as a material for fabricating MEMS sensors for high temperatures and harsh environments since the early 1990s [1]. Its excellent mechanical and chemical properties make it suitable for high temperature (>300°C) and corrosive environments, while the wide bandgap yields very stable electrical properties at elevated temperatures. It has an upper temperature limit exceeding 2500 °C, where it sublimates rather than melts. Most SiC-based sensors utilize piezoresistive or capacitive transduction mechanisms that require constant bias voltages.

Diamond exhibits similar physical properties to silicon carbide, but lacks commercially available diamond substrates. As a result, thin film polycrystalline diamond is deposited on silicon, limiting the full temperature range of devices [2]. In addition, diamond requires a passivation layer to prevent oxidation effects [3].

Sapphire has a high melting point, chemical inertness, known material properties and mechanical strength. The primary limitation of sapphire for MEMS devices is the lack of micromachining processes. Although mechanical structures have been formed using ultrafast laser ablation [4], it is limited to serial fabrication and is still largely a research topic.

AlN thin films have been a research topic as a high temperature compatible material since the early 1990's [5, 6]. AlN is a piezoelectric material, but is not part of the ferroelectric sub-class. Ferroelectric materials, for example lead zirconate titanate (PZT), need to be poled to orient the grains in the film and realize a net piezoelectric affect. As a result, ferroelectric materials depole at their Curie temperature and lose their piezoelectric behavior. In contrast, AlN is oriented as deposited and does not have a Curie temperature. Instead, AlN is limited by the temperature at which the chemical bonds begin to break down. The piezoelectric response of AlN has been measured out to 1150 °C [5]. Other AlN properties that are advantageous are a high thermal conductivity (320 W/(m·K)), high Young's modulus (345 GPa), high resistivity (10^{14} Ω·cm), and low relative permittivity (10.2). Although many studies have been performed to investigate thin film AlN properties at room temperature, Elmazria et al. [7] indicates "further studies to characterize AlN's acoustic and piezoelectric properties … at high temperature are necessary to conclude regarding its use in industrial scale."

By coupling AlN and SiC, we propose to leverage the high temperature piezoelectric response of AlN with the excellent mechanical properties of SiC. Thus, the advantages of SiC, including commercial availability of polySiC wafers and known micromachining techniques, can be coupled with piezoelectric transduction. The integration of these two materials into a MEMS

microfabrication process represents a major challenge. The below discusses the process development of the Sandia AlN-SiC MEMS, or XMEMS, process.

2. PROCESS FLOW

The following describes the fabrication flow that was developed for the XMEMS process. The materials in the layer stack were consolidated to minimize device curvature induced by differences in thermal expansion coefficient. This includes the use of nitrogen-doped SiC (SiC:N) as the electrode material for the AlN. Metal materials with similar thermal expansion coefficient, such as molybdenum, are possible substitutes as electrode materials. For this work, we were restricted to a limited number of metal electrode options available in our CMOS silicon fabrication facility, none of which were both high temperature compatible and could serve as a good substrate surface to promote highly (002) oriented AlN. The doped SiC is an option compatible with our CMOS facility and has the added benefit of maintaining a consistent material set between the substrate, structural layer, and electrodes. The drawback is that, as will be shown in the following section, a thin plasma enhanced tetraethylorthosilicate (PETEOS) was required to achieve highly (002) oriented AlN. Although this layer is decidedly mismatched in thermal expansion, its thickness is relatively small in comparison to the other layers (0.05 μm as compared to a total of approximately 2.35 μm).

The following fabrication steps refer to Figure 1. (a) The substrate is a polycrystalline SiC wafer. (b) A low stress silicon nitride is deposited and patterned using an oxide hard mask. (c) Afterwards, the SiC is etched approximately 4 μm using the oxide as the mask layer. This etch forms the sacrificial trench that is used to release the devices. The oxide hard mask is removed post-etch. (d) A poly-silicon sacrificial layer is deposited to fill the trench in the SiC. (e) The poly-silicon is patterned to increase the speed and uniformity of planarization. (f) A chemical mechanical polish (CMP) is performed to planarize the poly-silicon down to the silicon nitride etch stop. (g) The silicon nitride is removed via a wet etch. (h) A 2 μm thick polySiC structural layer is deposited. A CMP is performed to reduce the SiC roughness to 10 nm RMS. (i) A 300 nm SiC:N is deposited to form the bottom electrode. A CMP is performed to reduce roughness to 1 nm RMS. The reduced roughness is needed to promote proper crystal alignment during the AlN deposition. (j) The SiC bottom electrode is patterned using an oxide hard mask. The surface resistivity is monitored to determine termination of the etch. (k) A 50 nm PETEOS is deposited to serve as a buffer between the doped SiC and AlN to enhance crystal orientation. (l) A highly (002) oriented, 750 nm AlN film is sputter deposited. (m) A via is etched through the AlN and PETEOS films to the bottom SiC electrode. (n) A 300 nm SiC:N film is deposited to form the top electrode. A CMP is performed to reduce roughness to less than 10 nm RMS. The top SiC:N electrode makes contact to the bottom SiC:N electrode through the via in the AlN. (o) The top SiC:N electrode is then patterned. (p) Release holes are etched through the SiC:N/AlN/SiO2/ SiC:N/SiC layers landing inside the poly-Si release pit. (q) Finally, the device is released using an isotropic xenon difluoride etch of the poly-Si.

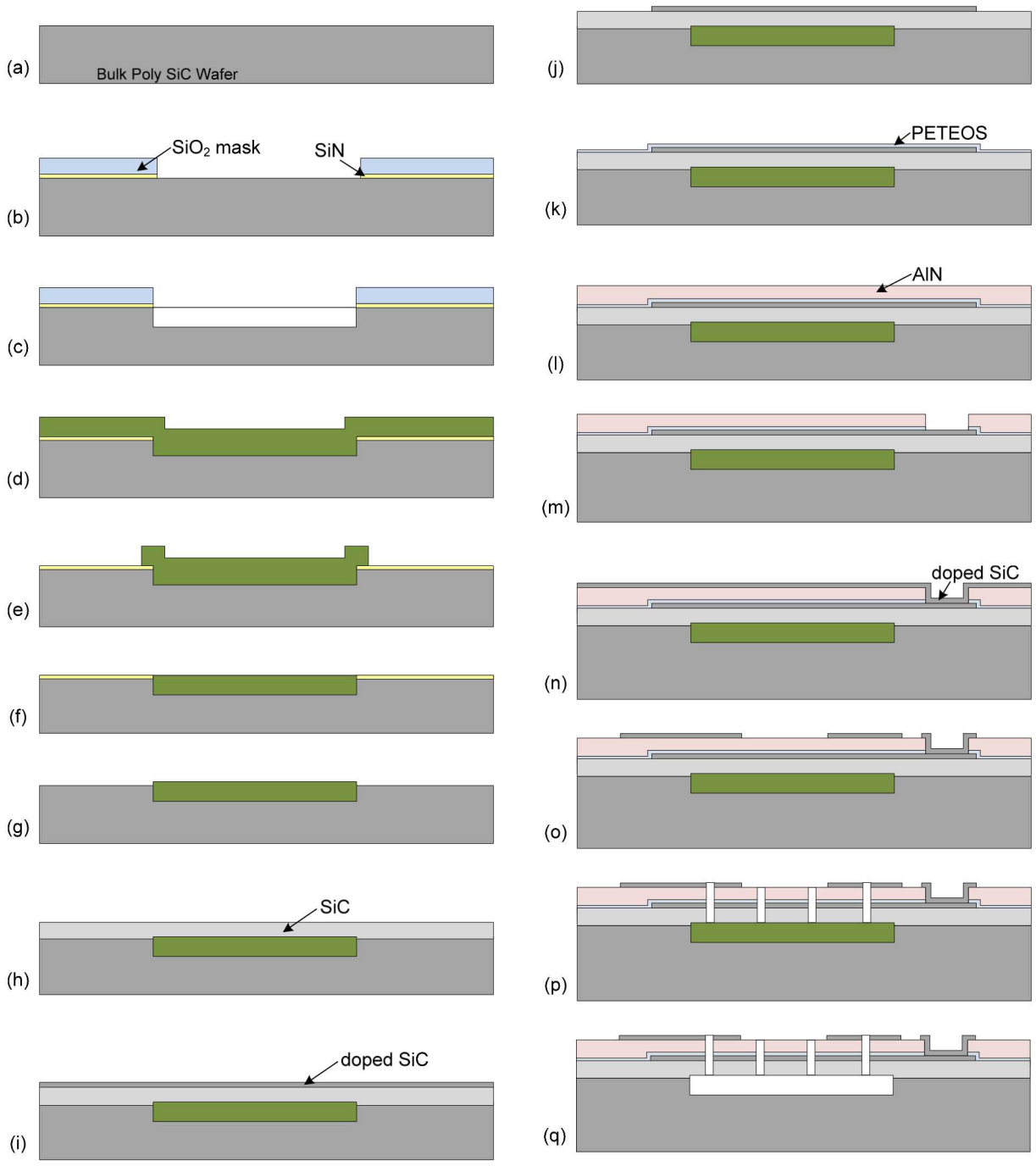

Figure 1. AlN/SiC MEMS microfabrication process flow.

3. COMPUTATIONAL MODEL

A Comsol model with temperature dependent material properties was developed as a part of this project. A piezoelectric diaphragm was used as the test model. The literature did not contain comprehensive measurements of material properties over the full temperature range of interest (1000 ˚C). Stiffness matrix measurements of AlN from 200 to 800 K were found in [8] and are shown in Table 1. Quadratic curve fits to the data were used to interpolate the values between the temperatures given. The thermal coefficients of expansion for the c and a crystal directions of AlN are also in Table 1 [9]. A linear curve fit was used to interpolate. The literature on the temperature dependent piezoelectric coefficients of AlN is sparse. Kano [10] reports that d_{33} is constant for 20-300 °C. Rossel [11] also notes that e_{31} has no temperature dependence up to 220 °C. As such, the temperature dependence of the piezoelectric coefficients was neglected.

Table 1. Temperature Dependent Material Properties of AlN.

	Temperature [K]	300	400	500	600	700	800
C_{11}	GPa	408.03	407.08	405.70	404.32	402.83	401.20
C_{12}	GPa	100.18	99.94	99.60	99.26	98.90	98.51
C_{44}	GPa	100.08	99.84	99.51	99.17	98.80	98.41
C_{13}	GPa	83.40	83.20	82.92	82.64	82.34	82.01
C_{33}	GPa	384.30	383.40	382.10	380.80	379.40	377.90
C_{66}	GPa	153.93	153.57	153.05	152.53	151.97	151.36
α_a	ppm/K	4.35	4.50	4.65	4.80	4.95	5.09
α_c	ppm/K	3.48	3.67	3.85	4.04	4.22	4.41

Similarly, the temperature dependence of SiC's thermal expansion coefficient and Young's modulus were included. The thermal expansion coefficient and Young's modulus are given in Table 2 [1]

Table 2. Temperature Dependent Material Properties of SiC.

	Temperature [K]	300	400	500	600	700	800
E	GPa	330.8	329.7	328.7	327.9	327.1	326.3
α	ppm/K	3.27	3.59	3.87	4.11	4.31	4.47

The model calculates the center deflection of the diaphragm as a function of voltage and pressure at temperature. The deflection per pressure is an indication of the sensitivity of the diaphragm acting as a microphone. The deflection per voltage is an indication of the sensitivity of the diaphragm acting as an actuator. The plate is assumed axi-symmetric with clamped boundary conditions. An annulus of AlN exists on the edge of the SiC plate such that the areas of the circular plate with and without AlN are equal. The bottom of the AlN is the ground plane such that the actuation voltage is applied to the top. For the following results, electrodes of different material composition are neglected for simplicity, but can easily be added.

An example of the deflection mode shape with a quarter cut-away is shown in Figure 2. In Figure 3 and Figure 4 are deflection results as a function of applied voltage and pressure, respectively, for room temperature and 800 K. Note that there are two 800 K results, one

showing the result not accounting for thermal expansion and the other including thermal expansion effects. Not that the sensitivity at room temperature and at 800 K are nearly the same when not including the thermal expansion effects. There is a large difference in the sensitivity when including thermal expansion effects. The effect is exaggerated since the edge of the diaphragm is clamped in the model. In reality, the edge of the diaphragm will expand with the temperature step and relieve some of the thermally induced stress in the diaphragm.

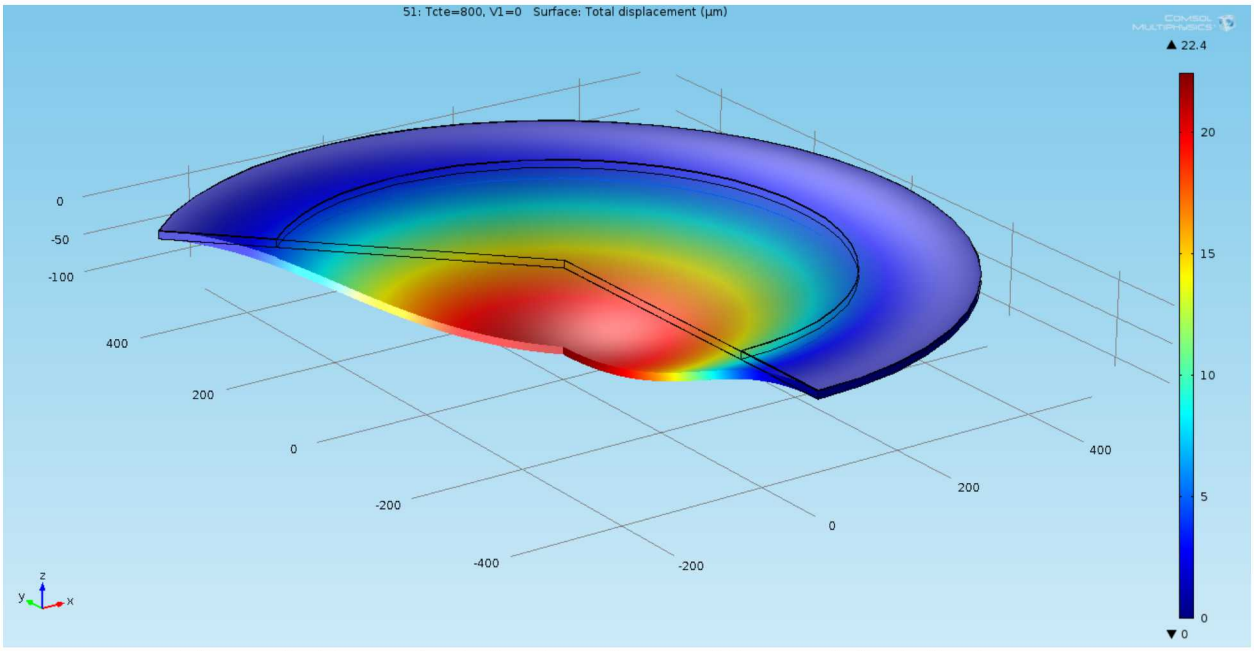

Figure 2. Example deflection shape of the modelled diaphragm.

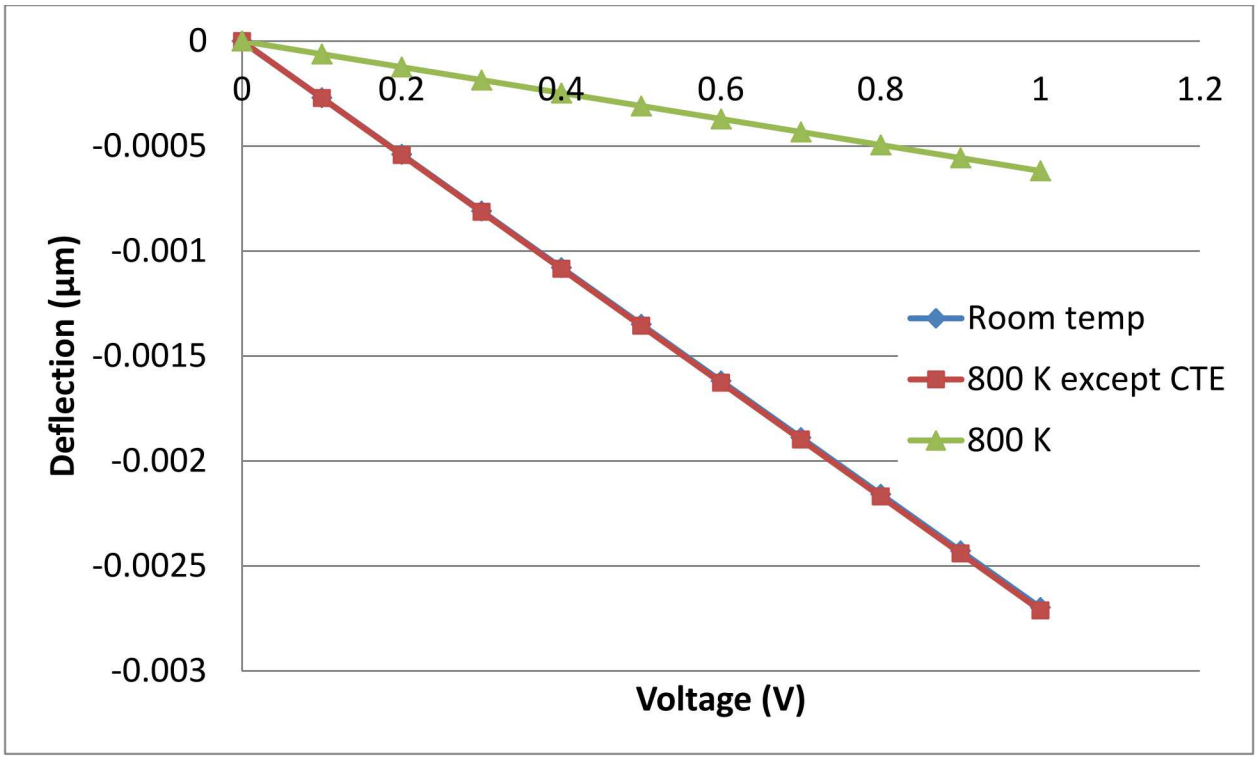

Figure 3. Center deflection of the diaphragm as a function of voltage application.

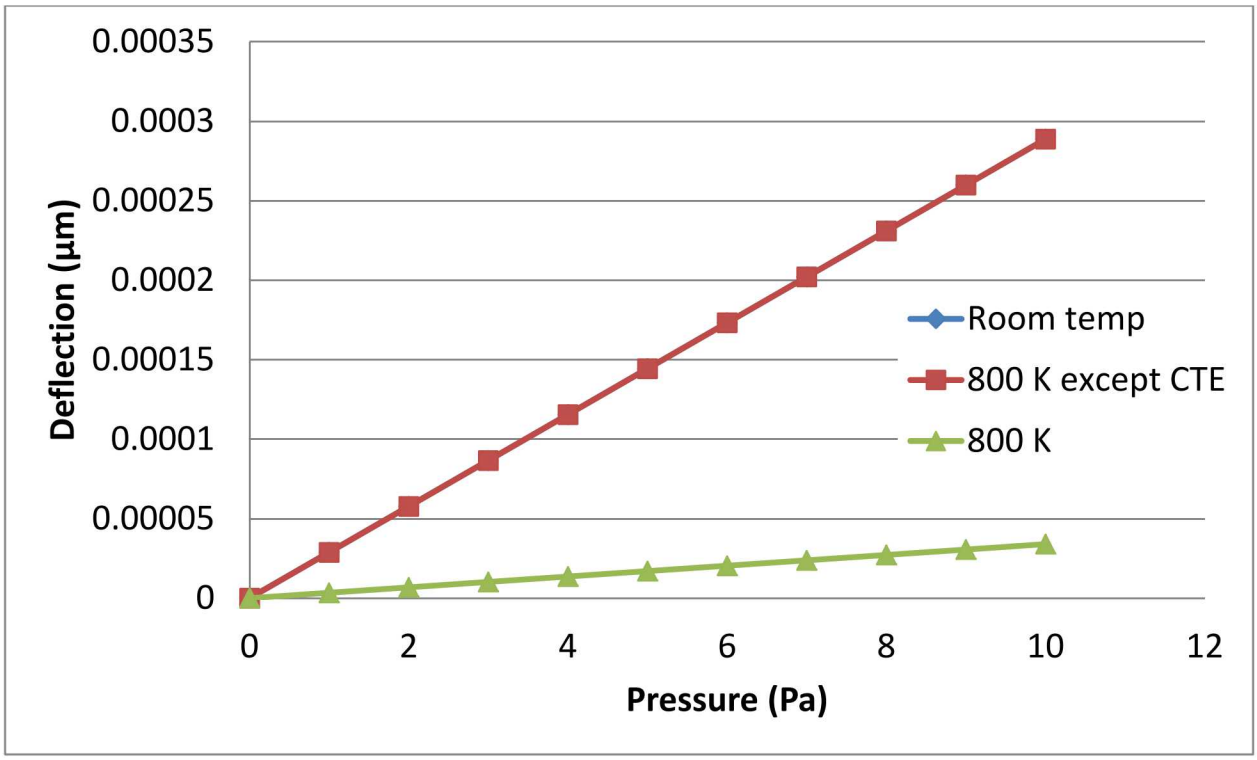

Figure 4. Center deflection of the diaphragm as a function of pressure application.

4. FABRICATION INTEGRATION

The following describes development of individual fabrication steps that are used in the overall process in Figure 1.

4.1 Silicon Carbide

A low pressure chemical vapor deposition technique (LPCVD) is used to form highly-textured hexagonal SiC (α-SiC) thin films. The LPCVD process entails the formation of α-SiC from a gaseous mixture of dichlorosilane (SiH_2Cl_2, or DCS) and dichloroethylene ($C_2H_2Cl_2$, or DCE) at temperatures in the range of 850 to 950°C and a pressure of approximately 250 mTorr [12]. Variation of the DCE/DCS flow ratio controls the residual film stress and structural polytype. Conditions of carbon saturation favor the formation of α-SiC and compressive stress, while silicon saturation conditions favor the formation of cubic SiC (β-SiC) and tensile stress [12]. These films are not doped and exhibit a very high resistivity.

Formation of the SiC:N electrode material is achieved through a variation of the process described above. Nitrogen is the most commonly used n-type dopant for SiC. Herein, conductive SiC:N is achieved by in-situ introduction of ammonia (NH_3) to the above-described process. NH_3 flow rates ranging from 0.2 to 2.0 sccm yield SiC:N resistivities from approximately 20 to $1x10^{-3}$ ohm-cm, respectively. The dopant activates in-situ and does not require an activation anneal. Films with a resistivity of 10^{-3} ohm-cm are degenerately doped and represent an upper bound to the conductivity of SiC:N produced by this process. In fact, for NH_3 flows approaching 5.0 sccm the SiC:N resistivity increases, presumably due to the matrix formation of dielectric silicon nitride. A cross-section SEM of the SiC:N is shown in Figure 5. Note the roughness of the as deposited SiC is approximately 50 nm RMS and thus requires a CMP process to smooth the film.

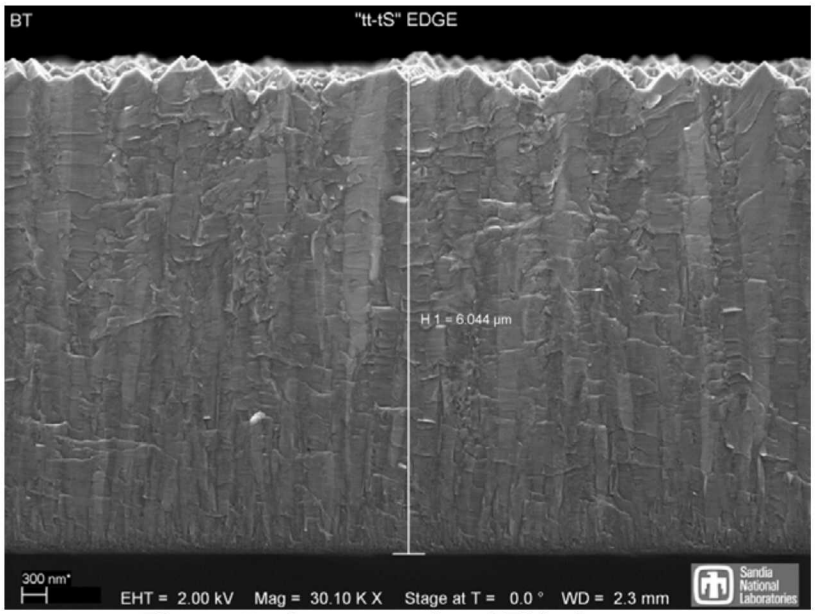

Figure 5. Cross-section SEM of SiC:N.

4.2 Aluminum Nitride

The AlN used in this work was deposited by pulsed DC reactive sputtering of aluminum in nitrogen and argon at 350 °C. The sputter deposition is manipulated via pressure, substrate temperature, and RF bias as well as substrate material and roughness to achieve highly (002) oriented AlN. A cross-section SEM of AlN deposited on silicon is shown in Figure 6. The vertical grains indicating good orientation is clearly seen. X-Ray diffraction measurements of AlN on silicon indicate a full-width-half-maximum of 1.5° indicating strong (002) orientation.

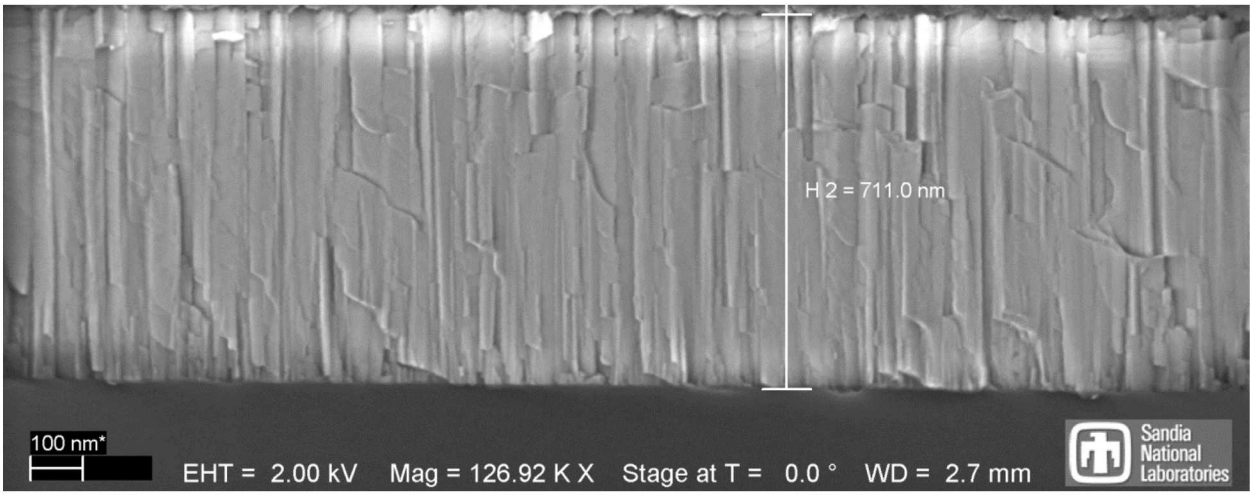

Figure 6. Cross-sectional SEM of (002) oriented AlN deposited on silicon.

One of the first experiments conducted to show integration of AlN into a high temperature process was to anneal it at high temperature and check that its crystal orientation is maintained. The AlN needs to survive high temperatures during sensor operation, but also the SiC top electrode deposition which is as high as 950 °C. A 750 nm thick AlN film on a titanium/titanium nitride bottom metal electrode was annealed at 950 °C for 3 hours in flowing nitrogen. X-Ray diffraction measurements were used to determine the crystal alignment before and after the anneal. The full-width-half-maximum (FWHM) showed near negligible shift from 1.8° to 1.7°, proving that the crystal alignment was at least maintained or slightly improved Figure 7.

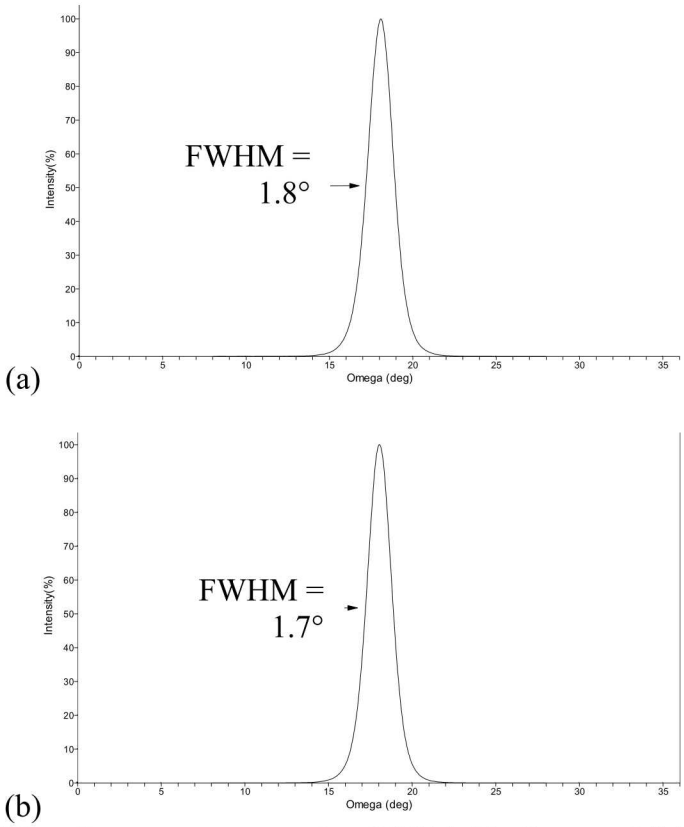

Figure 7. X-Ray diffraction measurements of AlN (a) before and (b) after annealing at 950 °C.

4.3 Integrating AlN and SiC Films

In order to successfully integrate doped-SiC electrodes, the AlN film needs to be able to withstand the conditions of the SiC deposition. Thus, we deposited a SiC film on an AlN film to simulate this step in the fabrication process. The resulting cross-section is shown in Figure 8. As you can see, the integrity of the AlN grains appear intact despite the 950 °C processing temperature of the SiC LPCVD. In addition, a CMP has been performed on the SiC surface. The success of the CMP is essential so that further processing can be completed on the films. No delamination between the films was observed after the CMP.

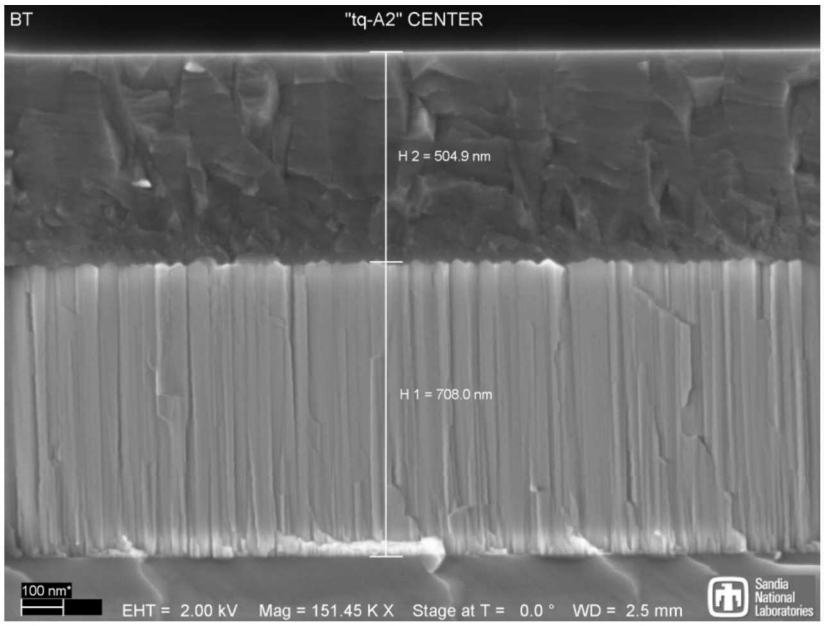

Figure 8. SiC film deposited on AlN. A CMP has been performed to smooth the SiC surface.

As discussed previously, the orientation of the AlN grains is highly dependent upon the substrate material. AlN was deposited on a SiC film to see what level of AlN crystal orientation could be achieved. A CMP was performed on the SiC surface prior to deposition to reduce the roughness to approximately 1 nm RMS. A transmission electron microscopy (TEM) image of the films' cross-section is shown in Figure 9. To the naked eye, the AlN grains appear fairly columnar. X-Ray diffraction measurements, however, showed a FWHM of 10.8° (Figure 10a). To enhance the AlN orientation, a 50 nm PETEOS buffer was deposited onto the SiC electrode before the AlN deposition. This improved the FWHM to 1.7° (Figure 10b), an orientation that will yield superior piezoelectric properties.

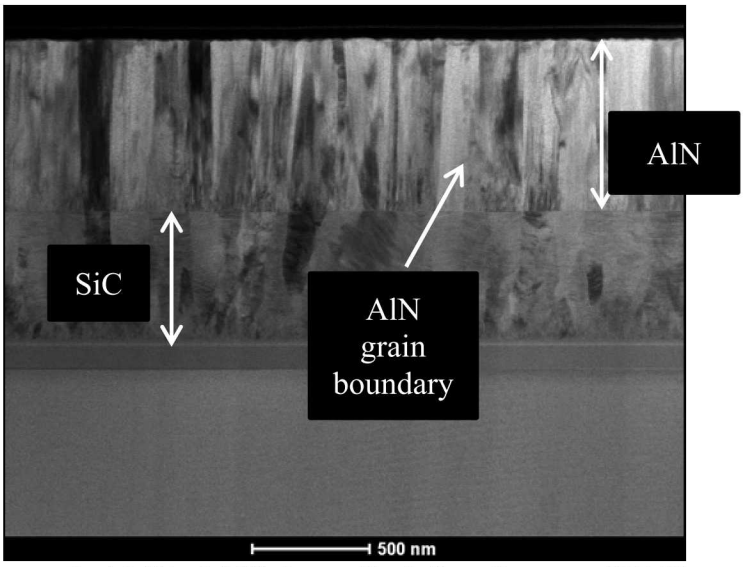

Figure 9. TEM of AlN deposited directly on a SiC film.

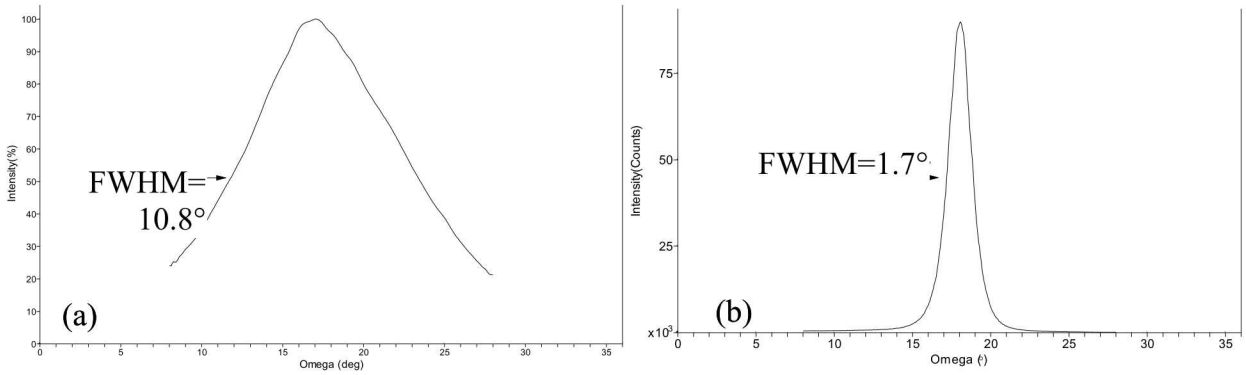

Figure 10. X-Ray diffraction measurements of AlN deposited (a) directly onto the SiC film and (b) using a 50 nm PETEOS buffer.

4.4 Film Stress

When integrating films and process steps to create a surface micromachined process, it is important to measure the film stress. The stress of each film is more times than not dependent upon not only the deposition conditions but also the underlying substrate. Therefore, the stresses of each film were measured as they were deposited on the underlying film in the stack using a Frontier Semiconductor (FSM) 128C2C non-contact full wafer stress mapping system. The FSM measures local wafer slope using an optical method. The radius of curvature is the slope of the linear line fit of the data. The film stress is calculated from the radius of curvature via Stoney's formula [13]. Three line scans were taken to achieve an average stress. Both TiN and SiC:N electrode stacks were studied. As can be seen in Table 3, the AlN film stress varies greatly between the SiC:N and TiN electrode options. The substrate upon which the AlN is deposited determines its nucleation which will effect grain growth and the resulting film stress. The average stresses of both film stacks are manageable with a -60 MPa average stress for the SiC:N electrode and 120 MPa average stress for the TiN electrode. Note that the top electrode was not measured for the AlN case, but it is expected to have a minor effect due to its relative small thickness.

Table 3. Film stresses for two different electrode options.

SiC:N Electrode		TiN Electrode	
2,000 nm SiC	-80 MPa	2,000 nm SiC	-80 MPa
300 nm SiC:N	30 MPa	20/25 nm Ti/TiN	-210 MPa
50 nm PETEOS	80 MPa	750 nm AlN	670 MPa
750 nm AlN	40 MPa	Average Stress	120 MPa
300 nm SiC:N	-280 MPa		
Average Stress	-60 MPa		

5. EXPERIMENTAL RESULTS

A variety of devices were simultaneously fabricated in the TiN process flow to explore the fabrication process and show functionality. The objective of the first fabrication run was to prove the fabrication process rather than to build a specific device. Both bending mode devices, such as diaphragms and cantilevers, as well as extensional mode devices, such as microresonators and phononic crystals, were fabricated. A few example measurements to show functionality are given below.

5.1 Ultrasonic Transducer

First, an ultrasonic transducer consisting of a diaphragm was created that has continuous bottom electrode and an annulus of top electrode. Thus, the application of voltage will create stress in the annular region of the AlN via the indirect, d_{31} piezoelectric effect. The stress will induce a bending moment causing deflection or, via an ac voltage, vibration of the diaphragm. An SEM image is shown in Figure 11. Note that the diaphragm is perforated with holes to allow for final device release. The size and number of holes was conservatively large to ensure the device was released in the initial fabrication run. Note that there is a bit of residue on the device as a result of a protective film applied during dicing. It is expected that this will be easily removed in future devices.

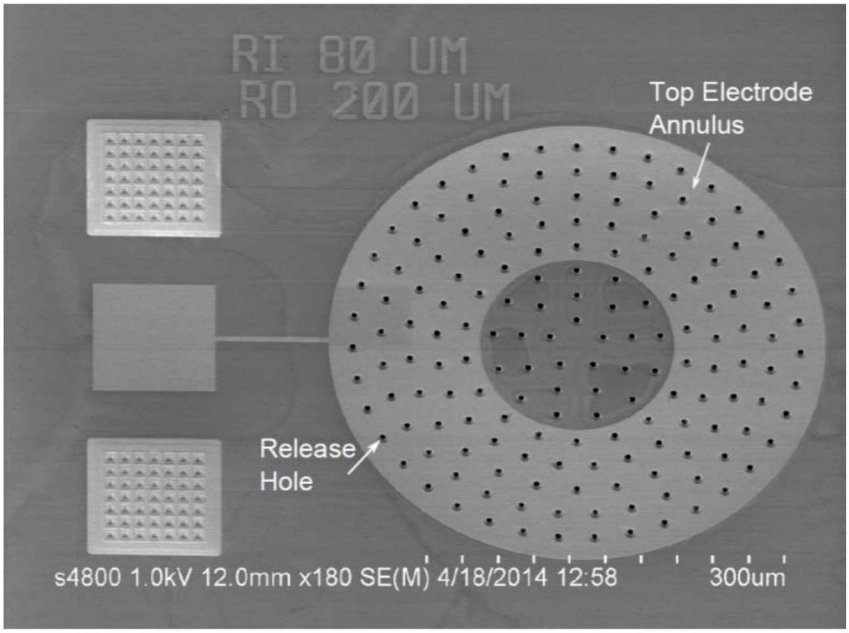

Figure 11. Piezoelectric ultrasonic transducer manufactured using the XMEMS process.

Vibration of the diaphragm was measured using a Polytec MSA 400 laser scanning vibrometer. The laser was scanned across the diaphragm to capture the fundamental mode shape at 513 kHz as shown in Figure 12(a). The frequency response of the center deflection per voltage is shown in Figure 12(b). The maximum deflection sensitivity at resonance is 30 nm/V.

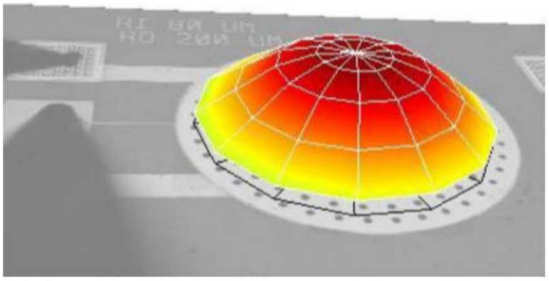

(a) Vibration mode shape at 513 kHz.

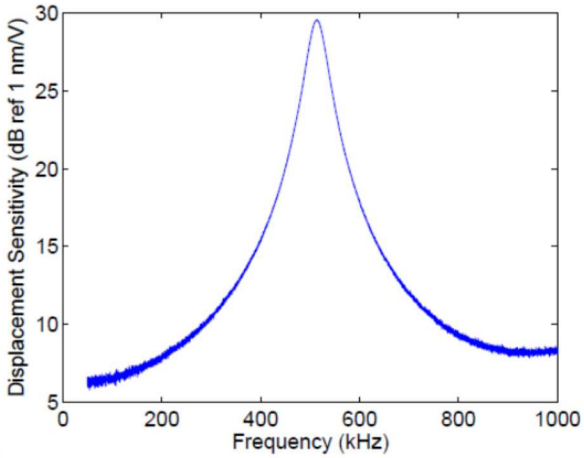

(b) Center point frequency response of the displacement sensitivity around the first resonant frequency..

Figure 12. Vibration measurement results of diaphragm driven by piezoelectric annulus.

A second ultrasonic transducer shown in Figure 13 was used for annealing studies. The transducer can be actuated using either the outer annulus electrode or the inner circle electrode. The outer diameter of the diaphragm is 200 μm and the inner diameter between the annulus and circle is 80 μm. The diaphragm was exposed to a series of rapid thermal anneals (RTAs) at increasing temperature and tested afterwards to show survival and the effect of the temperature exposure. During the RTA the chamber with the device was purged with argon and held at a pressure of 1 Torr. The temperature was held from two to seven minutes depending upon the recipe.

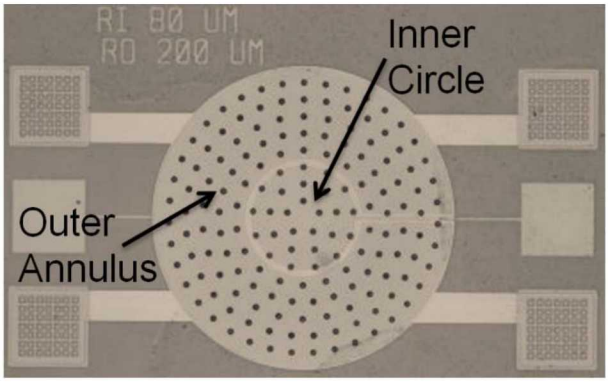

Figure 13. Ultrasonic transducer with inner circle and outer annulus electrode actuation.

The device response for both the inner circle electrode and the outer annulus electrode are shown in Figure 14. The resonant frequency decreases from the initial measurement to 500˚C. As shown, the inner circle electrode actuation response increases, whereas the outer annulus electrode response decreases. This device behavior is likely due to a shift in film stress, leading to a decrease in the resonant frequency. From 500˚C to 935˚C, the resonant frequency increases. In this temperature range, a different film is likely shifting stress and dominating the device performance. The most important result of this test is that the device survived a 935˚C anneal.

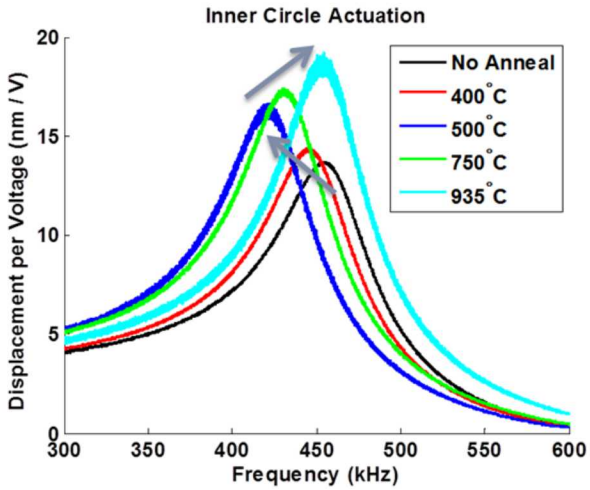

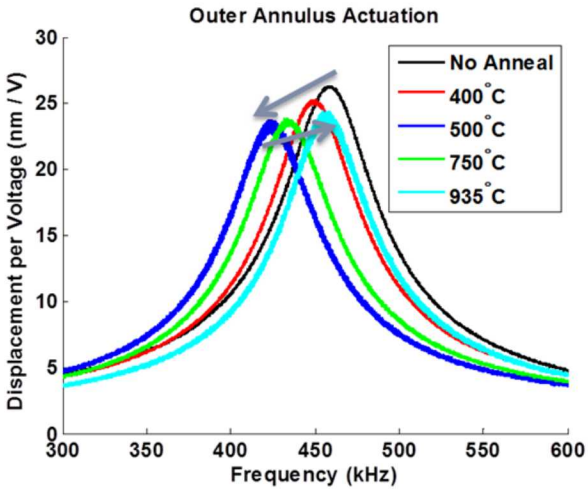

(a) Inner circle electrode actuation. **(b) Outer annulus electrode actuation.**

Figure 14. Ultrasonic transducer response as a multiple RTA temperatures.

5.2 Microresonator

A microresonator operating as a contour-mode rectangular plate [14, 15] and its transmission response are shown in Figure 15. The contour-mode resonator has top and bottom electrodes that are continuous across the free-standing rectangular plate. Application of a voltage creates an electric field across the AlN layer. This results in lateral strain via the d_{31} piezoelectric effect and excites the resonator into a width- or length-extensional mode shape depending upon the rectangular dimensions and excitation frequency. The resonator in Figure 15(a) will favor the length extensional mode shape due to the anchors along the center axis of the plate. The resonator response in air is shown in Figure 15(b). The estimated resonant frequency is 30.75 MHz based on a speed of sound of 11.1 km/s derived from film thicknesses and material properties. The resonator response in air shows a resonant frequency of 30.66 MHz which is sufficiently well matched considering the uncertainties in film thicknesses and material properties.

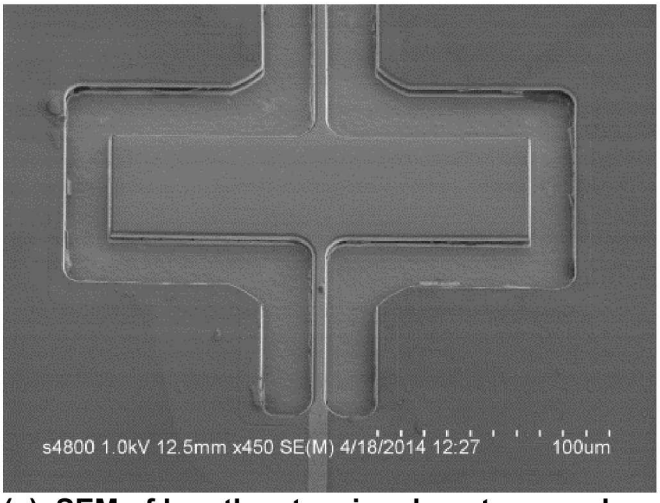

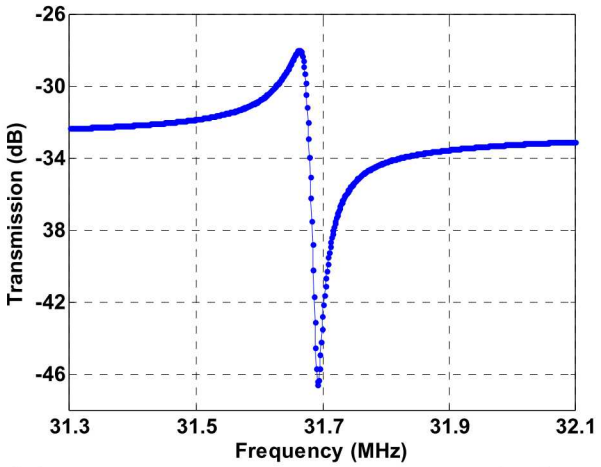

(a) SEM of length extensional contour-mode resonator. **(b) Resonator transmission with a Q of 363.**

Figure 15. Length extensional contour-mode resonator and measure transmission.

The quality factor (Q) given the transmission response in Figure 15(b) is estimated at 363. This is considerably lower than Q results (>2000) obtained in the low temperature AlN microresonator process at Sandia. This is due to the low conductivity of the TiN high temperature electrodes. The equivalent circuit model of the microresonator is shown in Figure 16, where M_M, C_M, and R_M are the motional inductance, capacitance, and resistance, respectively, C_{FT} is the feedthrough capacitance formed by the AlN in between the top and bottom electrodes, and R_L is the resistance due to the electrical lines. At resonance, the current bypasses the feedthrough capacitor and travels through the motional impedance. The reactance goes to zero and the motional resistance, R_M, would ideally dominate the device response. Due to low conductance of the electrodes, the line resistance, R_L, dominates the motional resistance and squelches the Q. To combat this, future devices could use electroplated platinum on the electrical lines to minimize the lead loss.

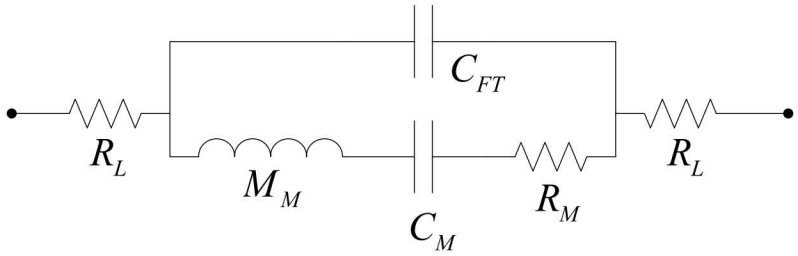

Figure 16. Equivalent circuit model of a length extensional contour mode resonator.

The length extensional contour-mode resonator was also exposed to rapid thermal anneals. Two separate device responses are shown in Figure 17, one taken to 750˚C and the other to 935˚C. Unlike the ultrasonic transducer, there is no clear trend with these devices. The primary result here is that they survived high temperature anneals and in all cases saw a frequency shift of less than 3%.

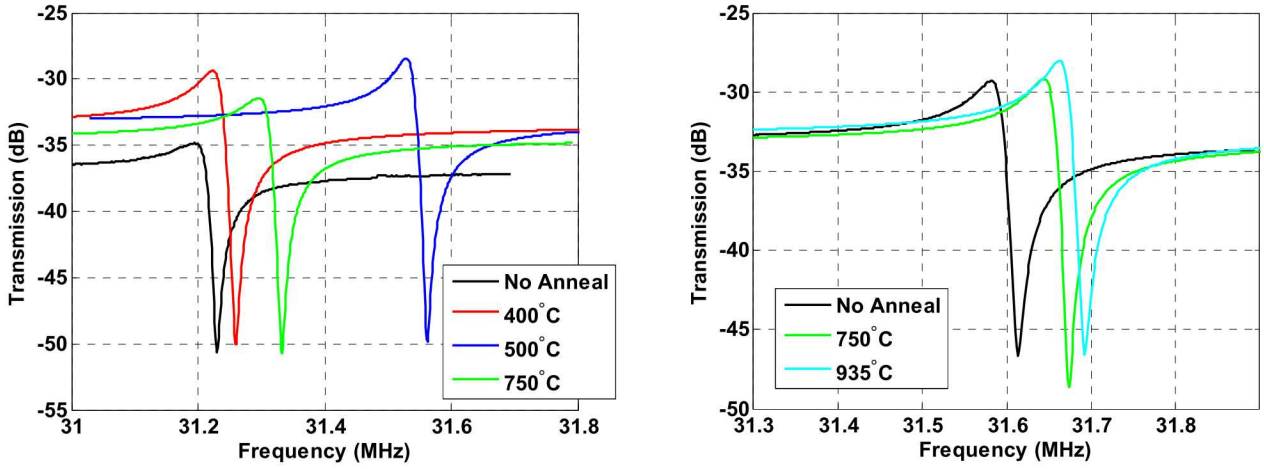

Figure 17. Length extensional contour-mode resonator response

6. CONCLUSIONS

In this work, we have shown functional devices fabricated in the XMEMS process which integrates AlN and SiC films on a poly-SiC wafer. We have measured maintained crystal alignment of AlN films after a 950˚C anneal. We have also shown a method to use a SiC:N film as an electrode material for AlN piezoelectric structures by using a PETEOS buffer. The device results show the fabrication process is capable of producing both bending mode structures and laterally driven microresonators. We have measured device response showing survivability post a 935˚C RTA. Future focus on this technology will revolve around creating high conductivity electrical lines to allow for higher Q microresonators.

7. REFERENCES

[1] M. B. J. Wijesundara and R. G. Azevedo, *Silicon Carbide Microsystems for Harsh Environments*. New York: Springer, 2011.

[2] E. Kohn, P. Gluche, and M. Adamschik, "Diamond MEMS — a new emerging technology," *Diamond and Related Materials,* vol. 8, pp. 934-940, 1999.

[3] P. John, N. Polwart, C. E. Troupe, and J. I. B. Wilson, "The oxidation of (100) textured diamond," *Diamond and Related Materials,* vol. 11, pp. 861-866, 2002.

[4] B. A. Griffin, D. A. Mills, T. Schmitz, and M. Sheplak, "A sapphire based fiber optic dynamic pressure sensor for harsh environments: fabrication and characterization," *49th AIAA Aerospace Sciences Meeting including the New Horizons Forum and Aerospace Exposition,* pp. 11 pp.-11 pp., 2011 2011.

[5] N. D. Patel and P. S. Nicholson, "High-Frequency, High-Temperature Ultrasonic Transducers," *NDT International,* vol. 23, pp. 262-266, Oct 1990.

[6] R. C. Turner, P. A. Fuierer, R. E. Newnham, and T. R. Shrout, "Materials for High-Temperature Acoustic and Vibration Sensors - a Review," *Applied Acoustics,* vol. 41, pp. 299-324, 1994.

[7] O. Elmazria and T. Aubert, "Wireless SAW sensor for high temperature applications: Material point of view," *Smart Sensors, Actuators, and MEMS V,* vol. 8066, 2011.

[8] D. K. Pandey and R. R. Yadav, "Temperature dependent ultrasonic properties of aluminium nitride," *Applied Acoustics,* vol. 70, pp. 412-415, Mar 2009.

[9] H. Iwanaga, A. Kunishige, and S. Takeuchi, "Anisotropic thermal expansion in wurtzite-type crystals," *Journal of Materials Science,* vol. 35, pp. 2451-2454, May 2000.

[10] K. Kano, K. Arakawa, Y. Takeuchi, M. Akiyama, N. Ueno, and N. Kawahara, "Temperature dependence of piezoelectric properties of sputtered AlN on silicon substrate," *Sensors and Actuators A: Physical,* vol. 130, pp. 397-402, 2006.

[11] C. Rossel, M. Sousa, S. Abel, D. Caimi, A. Suhm, J. Abergel*, et al.*, "Temperature dependence of the transverse piezoelectric coefficient of thin films and aging effects," *Journal of Applied Physics,* vol. 115, p. 034105, 2014.

[12] S. Habermehl, M. Rodriguez, and B. Simmons, "Formation of stress-controlled, highly textured, alpha-SiC thin films at 950 degrees C," *Journal of Applied Physics,* vol. 112, Jul 1 2012.

[13] D. Cheng, "System for measuring the curvature of a semiconductor wafer," United States Patent, 1993.

[14] G. Piazza, P. J. Stephanou, and A. P. Pisano, "Piezoelectric aluminum nitride vibrating contour-mode MEMS resonators," *Journal of Microelectromechanical Systems,* vol. 15, pp. 1406-1418, Dec 2006.

[15] M. D. Henry, J. Nguyen, T. R. Young, T. Bauer, and R. H. Olsson, "Frequency Trimming of Aluminum Nitride Microresonators Using Rapid Thermal Annealing," *Journal of Microelectromechanical Systems,* 2013.

8. DISTRIBUTION

1	MS0359	D. Chavez, LDRD Office	1911
1	MS0899	Technical Library	9536 (electronic copy)
1	MS1069	Benjamin A. Griffin	1719
1	MS1069	Eric D. Langlois	1719
1	MS1069	Michael S. Baker	2632
1	MS1069	Roy H. Olsson	1719
1	MS1072	Kenneth E. Wojciechowski	1767
1	MS1074	Travis Young	1746
1	MS1080	Keith Ortiz	1719
1	MS1084	M. David Henry	1746
1	MS1084	Peggy J. Clews	1746
1	MS1085	Tammy Pluym	1719
1	MS9106	Douglas L. Gehmlich	8226
1	MS9106	Jennifer Howard	8226
1	MS9106	Jonathan Ivers Helm	8226
1	MS9106	Bryan Loyola	8226

Sandia National Laboratories